Numerical analysis of complex patterns in drying liquid films

Fereydoon Taheri

Contents

1 Introduction **4**
- 1.1 Notion of instability phenomena and origin of formation of patterns . . . 4
- 1.2 Bénard intabilities . . . 7
  - 1.2.1 Rayleigh-Bénard convection . . . 7
  - 1.2.2 Marangoni effect . . . 8
- 1.3 Application-oriented aspects . . . 11

2 Mathematical description and the governing equations **13**
- 2.1 Dimensionless numbers and time scales . . . 13
- 2.2 Wavelength vs. depth . . . 15
- 2.3 Basic equations describing instabilities and the simplest case . . . 16

3 Swift-Hohenberg Equation **19**
- 3.1 General overview . . . 19
- 3.2 The numerical scheme . . . 21
  - 3.2.1 Implicit time-stepping . . . 22
  - 3.2.2 Internal iteration . . . 22
  - 3.2.3 Operator spliting . . . 23
  - 3.2.4 Spatial discretization . . . 25

4 Knobloch Equation **27**
- 4.1 Long-wave instability modes . . . 27
- 4.2 Fast Fourier Transform method . . . 29

5 Results **31**
- 5.1 Numerical results of Swif-Hohenberg equation . . . 31
- 5.2 Simulation results of Knobloch equation . . . 33

Prologue

More than a hundred years after Bénard discovery of cellular convective structures, the dynamics of pattern formation at interfaces is still one of the main subject of numerous studies over years. Consequently, constructing suitable mathematical models to explain thermal convection in fluid layers requires the understanding of the physics and the knowledge of length and time scales that characterize them regarding the fact that interfaces play a dominant role at small scales and their appropriate modelling is therefore of paramount importance in the rapidly expanding fields of nanotechnology and microfluidics (e.g. self-organized nano particle deposition patterns, quantum dots...).

In this study, after a brief discussion about the instability and origin of pattern formation and a succinct review of the application-oriented aspects of Bénard instabilities, we consider the case of surface-tension-driven instabilities. The latter leads to cellular structures in the form of hexagons in thin liquid films, known as Bénard-Marangoni convection, which has actually been much less studied than its buoyancy-driven counterpart. Then, an attempt is made to perform numerical simulations of the process of drying liquid films, using two different popular models, namely the modified Swift-Hohenberg equation and the Knobloch equation. In the first case, a new code has been developed based on semi-implicit finite difference scheme using operator-splitting and internal iteration, while in the second, an existing spectral code has been used. A comprehensive study of the outcome of these simulations will be done along with some qualitative comparisons with the experimental results. And finally a brief discussion of perspectives of this through study will be presented at the end.

1 Introduction[1]

1.1 Notion of instability phenomena and origin of formation of patterns

If a system is successively displaced from its equilibrium state by external forces, the homogeneity of the equilibrium state would be continuously replaced by an inhomogeneous non equilibrium state (**Reference state**). It is possible to describe such phenomena by defining the fluxes and the dissipation rate as a function of the imposed constraint existing over all the system. This function may account for the linear response of the system to the driving external gradients and can be characterized by parameters called **Control Parameters**. In such situations linearity will be sustained in a close vicinity of the equilibrium. Therefore although the system as a whole is in a non-equilibrium state the deviation from equilibrium stays sufficiently small for the system to be described as an ensemble of the infinitesimal volume elements locally at equilibrium (even though the system still is in non-equilibrium macroscopic scale) but corresponding to infinitesimally different values of the state variables [7]. These volume elements thus exchange energy and matter through their fictive boundaries, producing a flux throughout the system. Such situation can be regarded as **weak non-equilibrium** [1] or **sustained non-equilibrium** [15].

Reference states, existing in the case of weak non-equilibrium similar to their equilibrium equivalents, are asymptotically stable. This means that they tend to be damped in time since fluctuations around the reference state would eventually die out due to dissipative mechanisms (heat conduction and viscous friction in the case of fluid dynamics) [1]. However if the constraints resulting in non-equilibrium state of the system increase further, nonlinearities of different origins will act stronger and overcome the linear behaviour of the system alongside of weakening the ability to dissipate the fluctuations. And above a certain critical value of the constraints some fluctuations will grow in time rather than decay, implying the loss of the stability of the non-equilibrium reference state. Such an instability usually will be followed by the appearance of new states of different nature which are not necessarily asymptotic stable.

Considering in the sense of dynamical systems [8], a phase space where the instantaneous state of the system can be interpreted as a point (describing some trajectory in the case of time evolution), a **bifurcation** in the system can be resembled as the qualitative change in the structure of the phase space. Given such an assumption then a **reference**

[1] Much of the content in this chapter owes to a book from Pierre Colinet, Jean Claude Legros and Manuel G. Velarde titled "Nonlinear Dynamics of Surface-Tension-Driven Instabilities" [1] and the lecture notes of Pierre Colinet published in another comprehensive book titled "Pattern Formation at Interface" [2]

state is a fixed point in the phase space which become unstable above the critical value of the constraint. It means some trajectory around the reference state does not have any tendency toward it anymore implying that after the bifurcation there will be some directions in the phase space along which the trajectory gets away from the fixed point toward either another fixed point(node), or a limit cycle (circle), or a more complex situation (focus), all of which formally called **attractor**. It is worth to mention that the dimensionality of the attractor in the phase space is much lower than the dimension of the space due to property of **contraction mapping** of the volumes in the phase space. Note that the new attractor that system will reach after a sufficiently long time will be independent of the initial conditions providing some simplification (setting aside some more complicated situations such as multistability) [1].

Such a description for **instability** can be generalized for a wide range of systems undergoing bifurcation and the same macroscopic properties have been recognized in seemingly unrelated disciplines like fluid mechanics, solid-state physics, biology, population dynamics and even epidemiology or economics [1, 10, 11, 14]. This is because although the details of the system are important to explain the process leading to instability, the new states resulting from bifurcation indeed exhibit macroscopic characters that are independent from the specific details of their microscopic behaviours. Therefore the similar regimes can be observed in different systems not being alike.

Figure 1.1: The flow of pedestrians in a crowded street which is self-ordered in lanes of people walking in opposite directions, ©Mousaïd et al (2009)

In fact, the newly formed states appear from the cooperative behaviour of the microscopic constituent of the system (for example the interaction between atoms in a material as a system in solid-state physics or interdependence of humans in a society [see Fig. 1.1]). These composers of the system are able to organize themselves on time and length scales that are macroscopic compared to the microscopic scales of their individual interactions. And the basic reason for the emergence of strongly correlated structures

and formation of patterns corresponds to the dependency of the fluctuations growth rate on their spatial structure in accordance with these macroscopic scales. For instance near the threshold very limited fluctuations can extract energy from the reference state to become fast enough for dealing with dissipation as a consequence such modes will strongly determine the appearance of the structures above the limits of instability. On the other hand their spatial structure is actuated by the symmetries underlying the system. [1]

The resulting structures manifest themselves into different types of patterns like stripes (roll patterns) or hexagonal cells. It might be of the interest of the reader to know that such kind of patterns have been observed in a variety of systems, from Buoyancy-driven roll patterns in simple Rayleigh-Bénard setup (which will be considered more in details in section §1.2.1), to the geological pattern in earth, from reaction diffusion systems to optical settings or solidification systems, from dry eye syndrome, to semiconductor processing etc. In some cases it is even possible to find a description for these geometrical phenomena in large systems using the simpler ones. As an example the convections caused by buoyancy in a fluid confined between two horizontal plane with different temperatures is also the origin of the formation of cloud streets [see Fig. 1.2, left] at the boundary of convection rolls in the atmosphere. Another interesting example is the similar polygonal patterns observed in the the drying of the thin liquid films which can be seen in a dried salty lake possibly as a result of concentration of minerals at the colder boundaries of polygons[see Fig. 1.2, right]. This implies the importance of the better understanding of the instabilities in apparently simple systems.

Figure 1.2: Left : Cloud streets due to buoyancy and shear stress of the wind, ©J. Master (2005). Right : Khor salt lake Isphahan, Iran. The deposited minerals formed polygonal patterns. ©Hamshahri online [34]

For this reason in the present academic work we intend to study more concretely the convective flow in fluid layers submitted to temperature or concentration gradients in order to have acquired more insight into the systems in non equilibrium state. The

ostensible simplicity of such thermal convection which bring the instabilities to the laboratory scale experiments, along with the complexity of the resulting patterns have made it a very attracting subject to study.

1.2 Bénard intabilities

1.2.1 Rayleigh-Bénard convection

Consider a layer of incompressible and Newtonian pure liquid bounded by two smooth flat horizontal plates whose dimensions are much larger than the fluid layers thickness, and maintained at two controllable different temperatures where the lower plate has the higher temperature (in other words heated from below or cooled from above e.g. by evaporation at a free surface). Due to the warmer region at the bottom of the layer (we consider the layer to be sufficiently thick) a localized fluctuation arises in a certain volume element and as the density is less than the upper part, which is unfavourable in the field of gravity, upward force on this fluid particle will induce by buoyancy[2] and therefore system enters in sustained non-equilibrium state. As soon as the temperature difference $\Delta T = T_{lower} - T_{upper}$ exceeds a threshold value (quantifiable with regard to the depth of fluids, viscosity, thermal diffusivity...[see 2.1]) the fluid particle will set into motion in the upward direction generated by the buoyancy and ascending to the colder region. On the other hand the cooler fluid with higher density will be descending motivated by gravity leading to breaking the natural symmetry of the system and destabilizing it. This is the origin of amplification which illustrate itself in the form of convective roll patterns [see Fig.1.3].

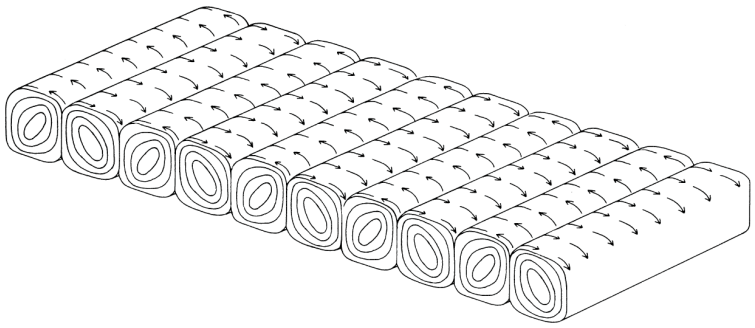

Figure 1.3: Roll patterns observed in Rayleigh-Bénard convection, the rolls are rotating in the opposite directions. ©extracted from [1]

Significant progress in the understanding of pattern formation in spatially extended systems has been possible thanks to well-controlled detailed experimental studies of the buoyancy-induced hydrodynamic instability (see e.g. the reviews [12]). Roll like cellular

[2]Buoyancy is an upward force exerted by a fluid that opposes the gravitational of an immersed object.

patterns and their transitions to more complex structures and turbulent-like behavior were indeed extensively studied, with or without additional effects [13], sometimes up to very high Rayleigh numbers.

Now in the following we will consider the case of thinner layer (the order of $1cm$ or less [1] where the buoyancy cannot be dominant) of liquid in contact with free surface[3] namely Bénard-Marangoni instability with a deeper look into the origin of such instability since it will be the main focus of this study.

1.2.2 Marangoni effect

Interfacial (surface) tension[4] at the boundary between two different fluid phases originates from the forces between molecules which are responsible for the cohesion of the condensed matter. In the case of a liquid-gas interface the molecules in the bulk of the liquid are attracted by their neighbours in an isotropic way (net force of zero) while those positioned on the interface have more tendency toward the liquid phase as they do not feel the presence of much more scattered molecules of gas. As a consequence they are pulled inward, create some **internal pressure** putting the system in a higher energy state which liquid tries to avoid by adopting a spherical shape to adjust the minimal area since according to **Laplace Law** the spherical shape minimizes the necessary "wall tension" of the surface layer for not being collapsed.

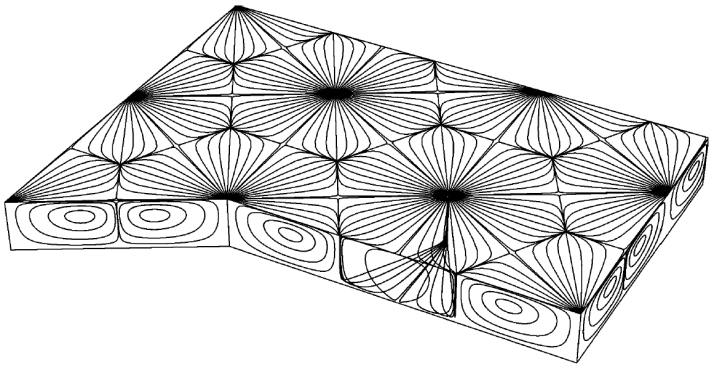

Figure 1.4: Hexagonal convection cells typical of Bénard-Marangoni convection. ©: the picture is extracted from [1]

Note that the surface tension is positive to be able to bring the molecules from the bulk of the liquid to the surface and it will generally decrease by the increase in the temperature in most liquids. Therefore if a fluctuation of temperature occurs at the interface the resulting imbalance between intermolecular forces will lead to a macroscopic tangential stress inducing a flow. This **thermocapillary flow** or **Marangoni flow** can be considered as a mechanism that system adopt to reduce the region with high surface

[3] the term "free" surface will be used for an interface between a liquid and a gas or a liquid and its vapor

[4] The energy necessary to create a unit surface area is called surface tension and denoted by σ.

tension by enlarging the low surface tension. It has to be noticed also provided that the surface tension gradients are the result of concentration differences along the surface of a mixture we will have **solutal Marangoni** (or **solutocapillary** effect) in the system. [2]

Nevertheless, considering a temperature fluctuation at the surface, a surface gradient is created and directed radially away from the fluctuation. Its associated shear stress (tangential stress) generates the divergence of the fluid motion on the surface, relaxing the instability at the point of disturbance. Simultaneously the continuity of the fluid cause a vertical ascending flow at the point of the disturbance. By increasing the temperature of the surface (heating from below) the surface tension will decrease so the tangential stress will increase and therefore after passing a critical value known as **critical Marangoni number** Ma_c (which again can be quantified by some properties of the liquid see 2.1) the surface fluid motions will organize themselves in mostly hexagonal patterns [Fig. 1.4].

Marangoni flows can be easily seen in our everyday life e.g. the motion of dusts in the wax of the candle due to proximity of the flame being at a much higher temperature compared to the edge of the candle. [2] or Formation of coffee rings at the bottom of a cup by Marangoni effect [Fig.1.2.2,left] due to the evaporation together with the influence of surfactants [20, 21]. Another famous example is the phenomenon of "tears of wine"[Fig. 1.2.2,right]. Although its mechanism is far more complicated engaging preferential evaporation of alcohol, wetting properties with glass, gravitational instability of fluid rising along the glass walls coupled with thermal and solutal Marangoni effect. James Thomson gave a tentative description of this phenomenon in 1855 even though Marangoni effect named after Carlo Marangoni's later work in 1870's. Henry Bénard though first observed hexagonal structures generated by Marangoni flows (thence called Marangoni-Bénard flows) in a fluid layer heated from below in 1901. However the correct interpretation of these patterns as the surface-tension-driven structures was given no sooner than 1956 experimentally by Block and theoretically by Pearson. [2, 16] This was the beginning of many further developments in fluid mechanics, yet many basic questions remain particularly in the case of high nonlinearity in the convection system when the Marangoni effect dominates.

For example taking into account some interesting experimental findings while the hexagonal patterns are typically observed in some range over the instability threshold, a transition from hexagons to squares patterns has been evidenced by Eckert et al. (inspired by the work of Nitschke) when the temperature gradient is increased. Such observation has suggested further theoretical researches by Thiele and Eckert, Eckert and Thess, Schatz et al., and Dondinger et al. Besides, Tokaruk et al. has also recognized square patterns in the case of substituting gas with liquid in the upper phase called **two layer** surface-tension-driven instabilities. In this case by increasing the constraint a transition to roll patterns occurs which is yet to be explained since it appears that buoyancy should not be the decisive element of the such phenomenon due to very small thickness of the liquid used in their experiment. [1]

Formation of dry spots and high spots in very thin liquid film of relatively viscous liquid heated from below is another fascinating finding by VanHook et al. Their work not only confirm the earlier theoretical prediction of the feedback of such a system to

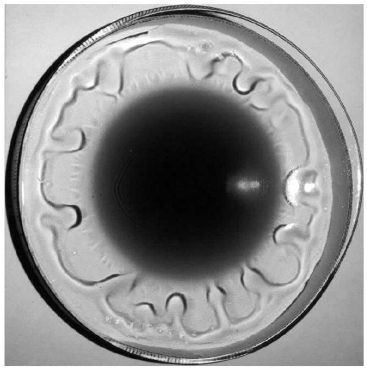

Figure 1.5:

Figure 1.6: Left:Dark rings at the bottom of the cup arising from Marangoni flow.[35] Right:Tears of wine. ©the picture is extracted from [2]

high surface deformation mode but also they have managed to demonstrate in more detail the role of the gas in this instability.

The last instance to be presented in this section and will be one of the main focus of this study is the experiment of Schatz who showed at very high supercriticality (see second chapter) the convection cells, along with attaining irregular polygonal shape, become time-dependent [Fig. 1.7]. The similar phenomenon has also been observed in mass transfer experiments.

Still as mentioned before several aspects of highly supercritical convection patterns (such as coarsening phenomena) are to be explained and might be the subject of future theoretical and experimental studies.

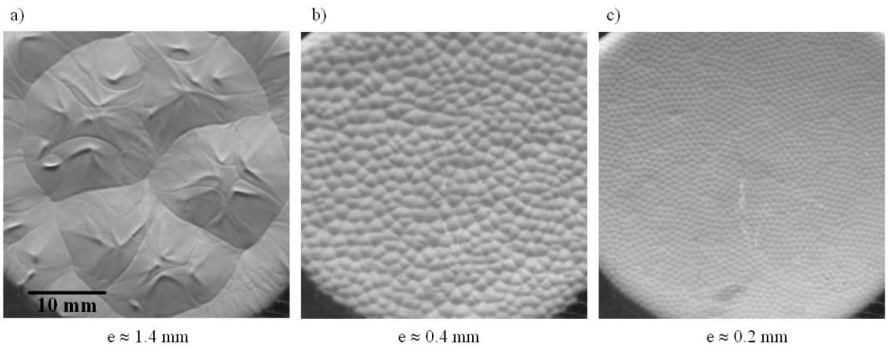

Figure 1.7: Time-dependent patterns generated during drying of a liquid film where e is the liquid thickness. ©: extracted from [31]

1.3 Application-oriented aspects

Beside the fundamental importance of Bénard instabilities in understanding of the pattern formations in vast array of sciences as mentioned before there are many practical application of such instabilities. In large scale, Rayleigh-Bénard convection for example is at the root of driving dynamics in the mantle of the Earth (plate tectonics). Moreover because the Earth is still geologically young, its interior has not yet cooled down and the flux of heat from its hot core out into space through its surface, together with heat received from the Sun, drives the dynamics of the atmosphere and ocean which are very determinant in the study of climate change. Buoyancy has also a major role in solar activity by by affecting the transport of heat from the center to the surface. [1, 15]

In the laboratory scale and industrial set-up, both buoyancy-driven and surface-tension-driven instabilities could yield desired enhancement in characteristics of heat/mass transfer. In fact, In numerous situations involving interfacial heat and mass transfer such as liquid-liquid extraction, gas absorption or deposition, distillation... order of magnitude change of transfer rates from one phase to another have been correlated with empirical relationships. Marangoni-Bénard convection is also important in the processes involving the phase changes (e.g. evaporation) such as drying of paint films in the coating industry and in heat exchanger based on the transport of heat (latent heat) by vapour (heat pipes). Convective cells reduce the overall thermal resistance of the liquid layer and as a result contribute to an increase of evaporation rate. Indeed the understanding of the basic mechanism of these pattern formations could lead to optimization of these empirical processes. (As they are dependent on properties such as direction of the transfer and bulk diffusivities, interfacial rheology, surface chemical reactions,...) The thin film evaporators are even used in the food and pharmaceutical industries where the liquid flowing on the heated plate may organize itself in the rivulet-like structures with the possible increase of the mass transfer rate in the regions where the layer becomes thinner. Although there is possibility of the appearance of dry spots. [24]

It also turns out that solutal Marangoni-Bénard convection has drawn out an growing interests nowadays in connection with the rapidly expanding areas of nanotechnology and microfluidics [16]. Indeed, the production of functionalized surfaces with desired properties is one of the aims of new technologies which often realized by a promising technique consists in spreading (e.g. by spin-coating) a thin film of a mixtures and allowing the solvent to evaporate leading to deposition of solute. The solute can be a substance which crystallizes and sediments above a certain concentration, a polymer which undergoes a glassy transition, or nanoparticles which cluster/aggregate and finally organize themselves during the deposition when the solvent fully evaporates. The implied coated surface thus will inherit some new properties from the solute such as optical, electrical, magnetic, wetting or other chemical properties. Recently a novel method also introduced by Majumder et al. [25] involving drop-drying of a suspension of nanoparticles in water in an ethanol vapour atmosphere which can be used for uniform depositing catalyst nanoparticles for the growth of single-walled carbon nanotubes as well as to manufacture plasmonic films of well-spaced, unaggregated gold nanoparticles. And finally the last application of interfacial instabilities to be introduced in this section is in

growing crystals onboard space laboratories (where the effect of buoyancy will considerably decrease). It was motivated by the researches started a few decades ago with the hope that weightlessness environment would allow constituting crystals of better quality compared to those grown on earth. Thus Instabilities of floating zone configuration and of half-zone model (liquid bridge) has been indeed extensively studied with regard to hydrothermal and surface instabilities.

2 Mathematical description and the governing equations

For the modelling of the liquid layer undergoing thermal/solutal Marangoni instability we can consider several different approaches. Starting from the smallest time and length scales, **molecular dynamics** will be a good option which certainly provide the most accurate description of interface structure and microscopic kinetics yet the computational costs of such techniques remains notably high, specially for polyatomic molecules. At intermediate (mesoscopic) level, there are methods based on **diffuse-interface** or **phase-field theory** which are numerically flexible for the problem involving complex dynamics. Another technique at same scale is **lattice Boltzmann** methods advancing on the basis of discrete models of celebrated Boltzmann equation and its variants which also characterize interface as non-zero thickness objects throughout which fluids experience sharp variations. Finally at the macroscopic level, interfaces are described as **zero-thickness** surfaces of discontinuity along which proper boundary condition should be expressed. There has been remarkable progresses in using this approach in last decades particularly in connection with nonlinear physics. Moreover these macroscopic models can be employed in very small scale even in submicrometer range. The latter will be the main approach of this study.

In the proceeding we will provide the general overview of the ingredients of the macroscopic modelling such as rescaling and dimensionless numbers.

2.1 Dimensionless numbers and time scales

To start with as we discussed thoroughly in chapter §1 we need to define the time scale in order to have the macroscopic view over the system. In fact several time scales can be introduced from the physical properties of the fluid and its spatial structure. For our goal we will first define a **thermal time scale**.

Thermal time scale is the time necessary for the temperature fluctuation in the fluid to be damped over a distance d.

$$\tau_{th} = \frac{d^2}{\kappa} \tag{2.1}$$

where κ is the thermal diffusivity of the pure liquid.(Note that $O(1)$ factors such as $4\pi^2$ are omitted in the previous relation and in what follows for the simplicity)

Similarly it is possible to define the time scale which can account for the damping of velocity fluctuation called **viscous time scale**. Namely the time it takes for the velocity

(or vorticity) fluctuation of the system to be decayed due to the viscosity of the fluid (ν) over the distance d.

$$\tau_{visc} = \frac{d^2}{\nu} \tag{2.2}$$

Two other time scales which do not depend on any molecular dissipation mechanism should be defined too. By using these time scales it will be possible to characterize the threshold above which the Bénard instabilities will occur.The first one is the time for the fluid particle at the bottom of the layer to be accelerated by buoyancy to the upper surface (**Buoyancy time scale**), i.e to a distance d

$$\tau_{buoy} = \sqrt{\frac{d}{\alpha g \Delta T}} \tag{2.3}$$

Note that in the equation 2.3, α is the thermal expansion coefficient of the fluid, g is the gravity acceleration and ΔT is the temperature drop across the layer of the fluid.

The typical time scale for the acceleration of the fluid particle along the interface is called **thermocapillary** or **Marangoni time scale** and is also defined as

$$\tau_{ma} = \sqrt{\frac{\rho d^3}{\gamma \Delta T}} \tag{2.4}$$

In the above equation, ρ is the volumic mass and $\gamma = -\dfrac{\partial \sigma}{\partial T}$ is the coefficient of the variation of surface tension with respect to temperature (positive for usual liquids).

Now we are able to find a criteria for the instability given the time scales introduced in this section. Since it is feasible to assume that instability will develop if the time for a fluid particle to cross some distance is shorter than the times necessary for the particle to either slow down by viscosity or thermally equilibrate with its surrounding. Therefore it is possible now to introduce dimensionless numbers accounting for Bénard instabilities.

Definition 2.1.1 (Rayleigh number)**.**

$$Ra = \frac{g\alpha \Delta T d^3}{\nu \kappa} = \frac{\tau_{visc}\tau_{th}}{\tau_{buoy}^2} \tag{2.5}$$

Definition 2.1.2 (Marangoni number)**.**

$$Ma = \frac{\gamma \Delta T d}{\rho \nu \kappa} = \frac{\tau_{visc}\tau_{th}}{\tau_{ma}^2} \tag{2.6}$$

These numbers are the usual measure for the description of destabilizing and stabilizing effects. Typically the critical value of the Rayleigh number above which the Rayleigh-Bénard instability appears is of order 10^3, while the critical Marangoni number is of order 10^2. Their actual values are dependent on the nature of the bed of the fluid and

the upper plate. (e.g. rigid and heat-conducting, or free and poorly-conducting) and must be determined by the instability analysis of the equations introduced in the next section (but the detailed derivation of these numbers is out of the scope of this thesis).

In the case of the presence of a free surface, the heat transfer through the gas is commonly considered to be described by a constant coefficient h (Its corresponding dimensionless number is Biot number $Bi = \dfrac{hd}{\lambda}$ where λ is the thermal conductivity of the body). Such approximation provides a qualitative description of the heat transfer influence on the interfacial dynamics. Actually the critical Marangoni number turns out to become greater if Biot number increases.

Another usual dimensionless parameter is **Prandtl number** which is defined as the ratio of the momentum and the thermal diffusivity and can also be written in the term of τ_{th} and τ_{vis}

$$Pr = \frac{\nu}{\kappa} = \frac{\tau_{th}}{\tau_{visc}} \tag{2.7}$$

Knobloch model, which is one of the simplified models for non-equilibrium patterns and will be extensively studied in chapter §4, will be effective in high Prandtl number in the modelling of highly viscous fluid. And other simplified model called Swift-Hohenberg may also derived from the fundamental equations of fluid dynamics which will be introduced in the next section in the limit of large Prandtl number. **Galileo number** is the last parameter to be presented in this section. It quantifies the proportion of gravity forces to viscous forces of the liquid and measures the stabilizing effect of gravity on the surface deformations.

$$Ga = \frac{gd}{\nu\kappa} = \frac{\tau_{visc}\tau_{th}}{\tau_{grav}^2} \tag{2.8}$$

Where $\tau_{grav} = \sqrt{\frac{d}{g}}$ is the gravity time scale which measures the time necessary for a body to travel over a distance d under the gravity acceleration.

Finally the notion of supercriticality should be mentioned for its importance in the mathematical modelling of Bénard type instabilities. Supercriticality ϵ is the measure of how far a system is above instability threshold after passing the critical it therefore for Marangoni-Bénard instability it will be

$$\epsilon = \frac{Ma}{Ma_c} - 1 \tag{2.9}$$

where Ma_c denotes the critical Marangoni number. Another interpretation of this parameter has been given in [1] as the proportion of the temperature drop of the system (ΔT) to the temperature difference at which the system became unstable for the first time (ΔT_c) hence $\epsilon_T = \dfrac{\Delta T}{\Delta T_c} - 1$

2.2 Wavelength vs. depth

The convective motions in the fluids embody themselves as superposition of waves existing in different directions hence concepts of length, periodicity and frequency will come

to the light for characterization of their behaviour and system self-organize itself in the form of a superposition of plane waves or Fourier modes (See later). On the other hand, as mentioned before, the depth of the fluid highly determines the nature of instabilities on the interface or inside the fluids. In general if the bed of the fluid is a good thermal conductor, polygonal convection cells of Marangoni-Bénard effect appear with a size proportional to the depth of the liquid layers.

On the contrary in the case that lower plate has a low heat transfer coefficient similar to the upper free surface, the horizontal length of the fluid motion generated by the temperature gradients will be much larger than the depth of the fluid hence the Marangoni cells also become large-scale which offers a way to describe them using **long-wave** asymptotic techniques. This method can be used for constructing relatively accurate simplified models for instabilities at some certain limits (using a multiscale long-wave expansion method).

This mechanism has some similarity with the formation of dry spot in a very thin liquid film [2]. The horizontal length of surface deformations in this case is also relatively larger than the liquid depth. This instability mechanism is called **long-wave deformation**.

However the derivation of the simplified models using this technique will not be discussed any further in these notes, it implies the importance of rescaling of the parameters to have a better view over the system.

2.3 Basic equations describing instabilities and the simplest case

The modelling of Bénard instabilities in a layer with the presence of surface tension ideally should involve the fluid motions and temperature fluctuation in both liquid and gas phases. Nonetheless it is possible to describe them with the only regard to liquid dynamics considering some simplifying assumptions and suitable boundary conditions. Such approach is called **one-sided modelling**. Therefore given the thermal time scale and dimensionless numbers introduced in 2.1, length scale d and pressure scale $\frac{\mu\nu}{d^2}$ and a temperature range θ, the basic dimensionless equations to describe thermally-driven Bénard instabilities read

$$\nabla.\mathbf{V} = 0 \tag{2.10}$$

$$\Delta\mathbf{V} - \nabla p - Ga\mathbf{1}_z\left(1 - \alpha\theta(T - \tilde{T}_r)\right) = Pr^{-1}\left(\frac{\partial\mathbf{V}}{\partial\tau} + (\nabla.\mathbf{V})\mathbf{V}\right) \tag{2.11}$$

$$\Delta T = \frac{\partial T}{\partial\tau} + (\mathbf{V}.\nabla)T \tag{2.12}$$

in which (2.10), (2.11) and (2.12) are mass conservation equation for incompressible fluids, momentum conservation and finally energy conservation of Navier-Stokes equations, respectively. In this system of equations, $\mathbf{V} = (U, V, W)$ denotes the velocity field, T is the temperature field and p stands for pressure field all of which are dimensionless. $\mathbf{1}_z$ is the unit vector along the z axis orthogonal to the layer and $\tilde{T}_r = \frac{T_{low} + T_{up}}{2\theta}$ is the

mean temperature at which the physical properties of the system are estimated (their possible variation is neglected over temperature change of θ).

It is also assumed[1] in this model that the density differences are sufficiently small to be neglected ($\alpha\theta \ll 1$) unless in terms containing the gravity acceleration. In other words gravity is sufficiently strong to make a specific weight appreciably different between two fluids. In equation 2.11, this fact can be seen knowing that Galileo number Ga is usually quite large (of order 10^8), such that $Ga\alpha\theta$ which is in face Rayleigh number (2.5) cannot generally be neglected.

It is worth to mention that an equivalent mathematical description can be considered for the case of mass transfer associated with **solutocapillary** flows disregarding some complications related to mass transfer through the surface such as accumulation of solute at the interface. Thereupon, in the simplest descriptions, essentially the pure fluid layer heated from below (or cooled from above) and the isothermal liquid layer encountering desorption through its free surface (or undergoing absorption of a soluble surfactant) are formally equivalent systems. Therefore it is possible to rearrange the equations 2.10-2.12 to have a simplified model for solutal Marangoni effect without loss of generality. It can be also applied to the simplified model to be discussed in §3 and §4 for modelling of the solutocapillary Marangoni flows.

The choice of boundary conditions will fully determine the specific Bénard set-up to be studied. In the simplest case, it is considered that on the bottom plate the temperature is constant and there exists no-slip condition hence

$$V = T - T_{bot} = 0 \qquad at \quad z = 0 \tag{2.13}$$

where $T_{bot} = \theta^{-1} T_{low}$. The free surface will be assumed at $z = 1$ therefore a coupling of gas and liquid phases is expected on the free surface. Hence the correct interpretation of the boundary conditions only in terms of liquid quantities at the interface is essential to construct a one-sided model. So first the surface is considered without motion thus the orthogonal velocity to the interface will be zero (we consider a non-evaporating case here)

$$W = 0 \qquad at \quad z = 1 \tag{2.14}$$

The next assumption is to take into account the surface tension gradients (due to temperature gradients) in the tangential stress balance. The gas viscous stresses in interface also can be neglected by considering the fact that the viscosity of the gas is much lower than the liquid. Therefore we have, in dimensionless form,

$$\partial_z U + Ma \partial_x T = 0 \tag{2.15}$$

$$\partial_z V + Ma \partial_y T = 0 \tag{2.16}$$

And finally by differentiating equation (2.15) with respect to x and equation (2.16) with respect to y and adding the result another boundary condition will be

[1] Boussinesq approximation

$$\partial_z^2 W = Ma\Delta T \qquad at \quad z = 1 \tag{2.17}$$

which follows from incompressibility equation 2.10. And $\Delta = \frac{\partial^2}{\partial x^2} + \frac{\partial^2}{\partial y^2}$ is the horizontal Laplacian operator. And finally assuming the heat transfer coefficient of the gas to be constant (Hence constant Biot number) the last condition yields

$$\partial_z T + Bi(T - T_\infty) = 0 \tag{2.18}$$

where $T_\infty = \theta^{-1} T_{up}$ is the temperature of the environment. There are other possible assumptions for more complicated situations by taking into account other effects e.g evaporation, gas thermal conductivity or presence of deformable interface. Linear stability analysis, matched-asymptotic expansion and Fourier transformation provide the helpful tools to deal with more complicated cases even analytically (please refer to [1, 2] for more detailed explanation of more complex situations), however it is generally impossible to solve the full system analytically even in the simplest case. Therefore for more realistic modelling of these instabilities numerical methods have proved to be useful.

The first way for numerical analysis of such systems is the direct numerical simulations considering the system of equations introduced earlier. However it appears to be remarkably time-consuming specially for three-dimensional simulations. Not only due to the need of finer mesh for capturing more details of the flow, but also because of the difference in time scales inherent to the the system. As an example near the instability threshold the evolution is quite slow (critical slowing down). Another difference of time scales is associated with the time for the system to be organized compared to the time for the convection cells to be shaped.

Studying simplified models of Bénard convection and pattern formation is another way to proceed in numerically studying the system. These models can be derived from the governing equations for instability such as those presented in this chapter within some asymptotic limits. The latter approach will be the main concern of this thesis in the following chapters.

3 Swift-Hohenberg Equation

3.1 General overview

Simplified models offer a deep insight in understanding the details of pattern formation observed in experiments without engaging the difficulty that exists in quantitatively accurate system of equations for the description of instabilities. Analytical and numerical calculation shows that if a simplified model contains some symmetries (rotational, transitional...), is characterized by a preferred length (and time scale) and has non-linearities that fully saturate the exponentially growing modes, it is able to reproduce the qualitative features of instabilities and in some cases quantitative details that have been evidenced in the experiments. [15] Another advantage of model equations is that they can usually be studied more thoroughly compared to the fully quantitative equations. Nevertheless model equations are much more important than being mathematically simpler and numerically faster to evaluate. And the most important feature of these models is their flexibility to be modified by different terms to test various hypothesises. Since they are often just based on symmetry and instability arguments and as a result they are not usually constrained by basic conservation laws of energy, momentum, and mass. (Although the details of the particular system should enter the numerical coefficients inside the model)

Swift-Hohenberg equation, as one of the prototype time evolution PDEs displaying formation of patterns, is one of such universal equations which was initially introduced by P. C. Hohenberg and J. B. Swift in 1977 [3] to describe the thermal convection in high Prandtl number and to account for the roll patterns seen in Rayleigh-Bénard instability. But later it has been adopted for the description of many different pattern formations. The different variants of it are widely used in different disciplines such as hydrodynamics (Couette flow, magnetoconvection,...) liquid crystals, flame dynamics, and nonlinear optics(see the references in [4]). This equation is derived from the basic equations presented in the previous chapter at some asymptotic limits (For heuristic derivation see [15]).

In this study the following Modified Swift-Hohenberg equation introduced in [2] will be considered

$$\partial_t \phi = \epsilon\phi - (\Delta + \mathbf{k}_0^2)^2\phi + \delta\phi^2 - \phi^3 \tag{3.1}$$

in which $\phi(\mathbf{r} = x\mathbf{1}_x + y\mathbf{1}_y, t)$ represents the two-dimensional free surface temperature field in a Marangoni-Bénard problem, ϵ is the supercriticality, and k_0 is the typical wavenumber of the system. The operator Δ is defined as $\frac{\partial^2}{\partial x^2} + \frac{\partial^2}{\partial y^2}$ and nonlinear part of the equation can be written as $F(\phi) = -\frac{d\Phi(\phi)}{d\phi}$ where Φ accounts for the potential of

the nonlinear force acting upon the system. Therefore

$$\Phi(\phi) = -\frac{\epsilon}{2}\phi^2 - \frac{\delta}{3}\phi^3 + \frac{1}{4}\phi^4 \tag{3.2}$$

When $\delta = 0$ this equation is the celebrated Swift-Hohenberg equation. For $\delta \neq 0$ equation(3.1) can be used for the simulation of Marnagoni convections, at least qualitatively.

Now consider the particular steady solution of the system $\phi = 0$. It can be regarded as non-equilibrium steady state of the system and can be treated as a reference state. For determining the stability of this state we perturb the system in the form of Fourier modes. Thus,

$$\phi(\mathbf{r}, t) = \eta \exp(\sigma_{gr} t) \exp(\mathbf{k}.\mathbf{r}) \quad \text{with} \quad \eta \ll 1 \tag{3.3}$$

In which σ_{gr} is the **growth rate** and $\mathbf{k} = k_x \mathbf{1}_x + k_y \mathbf{1}_y$ is a two-dimensional wave vector. Now inserting this solution into the linearised part of the equation yields the dispersion relation of the perturbations (i.e. $A = \eta \exp(\sigma_{gr} t)$)

$$\begin{aligned} & \partial_t A = \epsilon A - k^4 A - 2k^2 k_0^2 A - k_0^4 A \\ \Rightarrow \quad & \sigma_{gr} A = (\epsilon - k^4 - 2k^2 k_0^2 - k_0^4) A \\ \Rightarrow \quad & \sigma_{gr} = \epsilon - (k^2 - k_0^2)^2 \end{aligned} \tag{3.4}$$

which gives a relation between growth rate of the perturbation waves and their corresponding wavenumber $k = |\mathbf{k}|$. Similarly $k_0 = |\mathbf{k}_0|$. As it can be seen in Fig 3.1

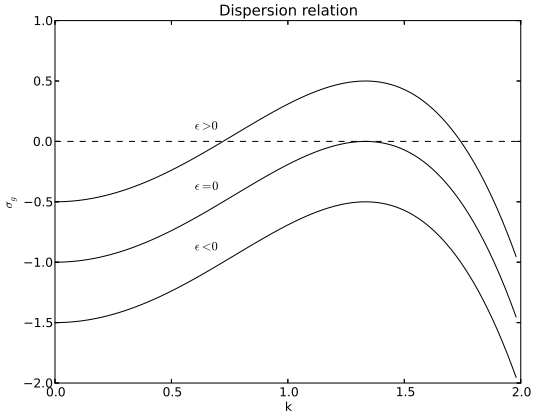

Figure 3.1: Dispersion relation of the Swift-Hohenberg equation

if $\epsilon < 0$ the reference state is stable since all Fourier modes have negative growth rate, thus corresponds to $Ma < Ma_c$ given the definition of ϵ. The case where $\epsilon = 0$ is the only situation where only one mode $k_c = k_0$ has a zero growth rate. Reference

state then is said to be **neutrally** or **marginally** stable. But a band of wavenumbers can be seen in the figure whose growth rates are positive, which shows the existence of instability. So if $\epsilon > 1$ some Fourier modes grow exponentially and the assumption of very small η in equation 3.3 is not anymore effective, and nonlinearity (ϕ^2 and ϕ^3) will act on the system, therefore coupling the Fourier modes. Thus patterns start to be formed. Note that at this stage the value of the parameters ϵ and δ will determine the nature of patterns to be formed. The study of their effect however is out of the scope of this work. Instead as mentioned in chapter §1 we attempt to use this model to capture the time-dependent convective cells which have been evidenced in the experiments by varying $\mathbf{k}_0$ and ϵ linearly in time.

An important feature of Swift-Hohenberg (afterward SH) model is that this equation possesses a Lyapunov functional which ensures the potential behaviour of the solution. Therefore the evolution of dynamics described by this equation will be always tend to a steady state monotonically by minimizing Lyapunov functional and the numerical approximation should satisfy this constraint on the solution. In the present work by using the numerical scheme proposed by Christov and Pontes in [5], a two dimensional semi implicit **finite difference** scheme of second order in time and space subject to **generalized Dirichlet boundary condition** will be presented. It will employ internal iterations to secure adequate approximation of the nonlinear term and it can be shown that the scheme satisfies a discrete approximation of Lyapunov functional (for more detail explanation see [5, 27])

3.2 The numerical scheme

For posing the problem[1] in domain D different type of physically acceptable boundary conditions can be imposed on the boundary of the domain ∂D. Let's first expand the equation 3.1 and rewrite it by denoting the non-linear part as $F(\phi)$

$$\partial_t \phi = -(\Delta^2 + 2k_0^2\Delta + k_0^4)\phi + F(\phi)$$

For finding the correct set of boundary conditions we consider the difference $v = \phi_1 - \phi_2$, where ϕ_1 and ϕ_2 are two solutions satisfying the same boundary conditions. By rewriting the equation 3.1 with respect to v, multiplying it by v and integrating over the domain it is possible to derive an **energy equation** as follows (n is the outward normal unit vector at the boundary)

$$\begin{aligned} \partial t \int \frac{v^2}{2} dxdy = & - \oint_{\partial D} 2k_0^2 v \frac{\partial v}{\partial n}\, dl + \oint_{\partial D} \Delta v \frac{\partial v}{\partial n}\, dl \\ & - \oint_{\partial D} v \frac{\partial \Delta v}{\partial n}\, dl + \int_D 2k_0^2 (\nabla v)^2\, dxdy \\ & - \int_D \Delta^2 v\, dxdy - \int_D k_0^2 v^2\, dxdy \end{aligned} \tag{3.5}$$

[1] Some notation used in this section is the same notation in [27, 5]

The correct set of b.c. is the one which secures the fact that the evolution of the energy is only dependent on its production or dissipation in the bulk of the fluid, but not on the surface. Therefore in 3.5 one has to make the surface integrals vanish. As a result the possible boundary conditions are

$$v = \frac{\partial v}{\partial n} = 0 \qquad v = \Delta v = 0 \qquad \frac{\partial v}{\partial n} = \frac{\partial \Delta v}{\partial n} \qquad x, y \in \partial D \tag{3.6}$$

$(3.6)_1$ and $(3.6)_2$ are called generalized Dirichlet conditions of first and second kind and $(3.6)_3$ which contain only derivatives at the boundary is generalized Neuman conditions. [3] Note that there is no restriction of using the mixed boundary conditions since any admissible mixture of boundary condtions introduced in 3.6 yields a well-posed boundary problem. For the sake of simplicity, we restrict ourselves to the generalized Dirichlet boundary condition of first kind $(3.6)_1$.

3.2.1 Implicit time-stepping

To ensure the potential behaviour of 3.1 by minimizing a monotonic functional, it is a priori clear that a scheme which is both implicit in time and nonlinear will possess the necessary symmetry to accommodate for this constraint [5]. For this reason an approximation for the nonlinearity also should be provided. Therefore our scheme reads

$$\frac{\phi^{n+1} - \phi^n}{\tau} = -\left(\Delta^2 + 2k_0^2\Delta + k_0^4\right)\frac{\phi^{n+1} + \phi^n}{2} - \frac{\Phi(\phi^{n+1}) - \Phi(\phi^n)}{\phi^{n+1} - \phi^n} \tag{3.7}$$

which can be expanded as

$$\begin{aligned}\frac{\phi^{n+1} - \phi^n}{\tau} = &-\left(\frac{\partial^4}{\partial x^4} + \frac{\partial^4}{\partial y^4} + 2k_0^2\frac{\partial^2}{\partial x^2} + 2k_0^2\frac{\partial^2}{\partial y^2} + 2\frac{\partial^4}{\partial x^2 \partial y^2} + k_0^4\right)\frac{\phi^{n+1} + \phi^n}{2} \\ &- \frac{\Phi(\phi^{n+1}) - \Phi(\phi^n)}{\phi^{n+1} - \phi^n}\end{aligned} \tag{3.8}$$

and hence the nonlinear potential term will adopt the form

$$\begin{aligned}-\frac{\Phi(\phi^{n+1}) - \Phi(\phi^n)}{\phi^{n+1} - \phi^n} = &\frac{\epsilon}{2}\left(\phi^{n+1} + \phi^n\right) + \frac{\delta}{3}\left((\phi^{n+1})^2 + \phi^{n+1}\phi^n + (\phi^n)^2\right) \\ &-\frac{1}{4}\left((\phi^{n+1})^3 + (\phi^{n+1})^2\phi^n + (\phi^{n+1})(\phi^n)^2) + (\phi^n)^3\right)\end{aligned}$$

3.2.2 Internal iteration

The internal iteration is used to deal with the nonlinearity of the scheme alongside with smoother handling of the inversion of linear operators in the case they are not negative definite. One should note that a simple consequence of the nondefiniteness of the linear operator is the occurrence of a linear bifurcation of the stationary problem. To face this complication we employ an explicit approximation of the second order terms.(Hence, the name semi-implicit method) An additional benefit of internal iteration method will

also be the possibility of using relatively larger time steps and hence decreasing the computational cost of the algorithm. Therefore we modify the scheme as follows

$$\begin{aligned}\frac{\phi^{n,k+1}-\phi^{n,k}}{\tau} &= -\left(\frac{\partial^4}{\partial x^4}+\frac{\partial^4}{\partial y^4}+k_0^4-\epsilon\right)\frac{\phi^{n,k+1}+\phi^{n,k}}{2} \\ &-\left(2k_0^2\frac{\partial^2}{\partial x^2}+2k_0^2\frac{\partial^2}{\partial y^2}+2\frac{\partial^4}{\partial x^2\partial y^2}\right)\frac{\phi^{n,k+1}+\phi^{n,k}}{2}+\frac{\delta}{3}\left(\phi^{n,k}+\phi^{n}\right)\phi^{n,k+1} \\ &-\frac{1}{4}\left((\phi^{n,k})^2+\phi^{n,k}\phi^{n}+(\phi^{n})^2\right)\phi^{n,k+1}+\frac{\delta}{3}(\phi^{n})^2-\frac{1}{4}(\phi^{n})^3\end{aligned} \tag{3.9}$$

where the superscript (n,k+1) denotes new iteration of the unknown function in the same time step, (n,k) shows the known quantity obtained from the previous iteration and (n) distinguishes the known value of the function from the last time step from which we can define $\phi^{n,0} \overset{\text{def}}{=} \phi^{n}$. The scheme with internal iterations is linear with respect to $\phi^{n,k+1}$ and the iterations will be conducted until the convergence is reached with following criterion

$$\frac{\|\phi^{n,K+1}-\phi^{n,K}\|_\infty}{\|\phi^{n,K+1}\|_\infty} < \delta' \qquad \text{where} \qquad \delta' \ll 1 \tag{3.10}$$

for certain K. And $\|.\|_\infty$ is **infinity norm** or Chebyshev norm which is for a given domain X defined as

$$\|x\|_\infty = \max_{i\in I}|x_i| \quad x_i \in X$$

Then the last iteration gives the sought function on the new time stage $\phi^{n+1} \overset{\text{def}}{=} \phi^{n,K+1}$. The number of iterations needed for convergence is very much dependent on the magnitude of the time increment of the scheme (τ). For smaller τ, the initial function of the iteration will be close to the sought function and the number of internal iterations is also expected to be small. Therefore for a very small time increment the computational cost will increase significantly for each nodal point of the grid. On the opposite for inappropriately large τ, number of internal iteration to reach one time step will increase heavily compelling the advantage of faster stepping in the time. This dependence between number of iteration and time increment is nonlinear and subject to another study for its optimization. In this simulation however based on the suggestion of Pontes and Cristov in [5] τ has been chosen to have at most 16 internal iterations and at least 4. Considering the time evolution of $\mathbf{k}_0$ in our simulation, even smaller steps in time have been used to catch the details of the faster time dependent systems.

3.2.3 Operator spliting

The inversion of the sparse matrix obtained from equation 3.9 is an expensive procedure as it is a **pentadiagonal matrix**. It becomes more problematic during the several repetition of computing the inverse matrix in every iteration in each time step. Therefore for minimizing the operations per unit iteration (hence per unit time step), an operator

splitting method is introduced as follows

$$\frac{\tilde{\phi}-\phi^n}{\tau} = L_{11}^{n,k}\tilde{\phi} + L_{22}^{n,k}\phi^n - \frac{1}{2}\left(\frac{\partial^4}{\partial x^4} + \frac{\partial^4}{\partial y^4} + k_0^4 - \epsilon - \frac{2\delta}{3}\phi^n + \frac{1}{2}(\phi^n)^2\right)\phi^n$$
$$- \left(L_1 + L_2 + L_{12}\right)\left(\phi^{n,k} + \phi^n\right) \tag{3.11}$$
$$\frac{\phi^{n,k+1}-\tilde{\phi}}{\tau} = L_{22}^{n,k}(\phi^{n,k+1} - \phi^n)$$

in which $L_{ij}(i,j \in [1,2])$ operators are defined as

$$L_{11}^{n,k} \stackrel{\text{def}}{=} -\frac{1}{2}\frac{\partial^4}{\partial x^4} - \frac{1}{4}k_0^4 - \frac{1}{8}\left((\phi^{n,k})^2 + \phi^{n,k}\phi^n + (\phi^n)^2\right) + \frac{\epsilon}{4} + \frac{\delta}{6}\left(\phi^{n,k} + \phi^n\right)$$
$$L_{22}^{n,k} \stackrel{\text{def}}{=} -\frac{1}{2}\frac{\partial^4}{\partial y^4} - \frac{1}{4}k_0^4 - \frac{1}{8}\left((\phi^{n,k})^2 + \phi^{n,k}\phi^n + (\phi^n)^2\right) + \frac{\epsilon}{4} + \frac{\delta}{6}\left(\phi^{n,k} + \phi^n\right)$$

$$L_{12} \stackrel{\text{def}}{=} \frac{\partial^4}{\partial x^2 \partial y^2} \quad L_1 \stackrel{\text{def}}{=} k_0^2\frac{\partial^2}{\partial x^2} \quad \textit{and} \quad L_2 \stackrel{\text{def}}{=} k_0^2\frac{\partial^2}{\partial y^2}$$

To show that the original scheme will be achieved through the splitting method let's rewrite the relation 3.11 as follows (E is unity)

$$\left(E - \tau L_{11}^{n,k}\right)\tilde{\phi} = \left(E + \tau L_{22}^{n,k}\right)\phi^n - \frac{\tau}{2}\left(\frac{\partial^4}{\partial x^4} + \frac{\partial^4}{\partial y^4} + k_0^4 + \epsilon - \frac{2\delta}{3}\phi^n + \frac{1}{2}(\phi^n)^2\right)\phi^n$$
$$- \tau\left(L_1 + L_2 + L_{12}\right)\left(\phi^{n,k} + \phi^n\right) \tag{3.12}$$

$$\left(E - \tau L_{22}^{n,k}\right)\phi^{n,k+1} = \tilde{\phi} - \tau L_{22}^{n,k}\phi^n \tag{3.13}$$

Now by applying the operator $\left(E - \tau L_{11}^{n,k}\right)$ to the equation 3.13

$$\left(E - \tau L_{11}^{n,k}\right)\left(E - \tau L_{22}^{n,k}\right)\phi^{n,k+1} = \left(E - \tau L_{11}^{n,k}\right)\tilde{\phi} - \left(E - \tau L_{11}^{n,k}\right)\tau L_{22}^{n,k}\phi^n \tag{3.14}$$

By replacing the term $\left(E - \tau L_{11}^{n,k}\right)\tilde{\phi}$ in (3.14) from the equation (3.12)

$$\left(E - \tau L_{11}^{n,k}\right)\left(E - \tau L_{22}^{n,k}\right)\phi^{n,k+1} = \left(E + \tau L_{22}^{n,k}\right)\phi^n - \tau\left(L_1 + L_2 + L_{12}\right)\left(\phi^{n,k} + \phi^n\right)$$
$$- \frac{\tau}{2}\left(\frac{\partial^4}{\partial x^4} + \frac{\partial^4}{\partial y^4} + k_0^4 + \epsilon - \frac{2\delta}{3}\phi^n + \frac{1}{2}(\phi^n)^2\right)\phi^n - \tau\left(E - \tau L_{11}^{n,k}\right)L_{22}^{n,k}\phi^n \tag{3.15}$$

Thus the result will be

$$\left(E + \tau^2 L_{11}^{n,k}L_{22}^{n,k}\right)\frac{\phi^{n,k+1}-\phi^{n,k}}{\tau} = \left(L_{11}^{n,k} + L_{22}^{n,k}\right)\phi^{n,k+1} - \left(L_1 + L_2 + L_{12}\right)\left(\phi^{n,k} + \phi^n\right)$$
$$- \frac{1}{2}\left(\frac{\partial^4}{\partial x^4} + \frac{\partial^4}{\partial y^4} + k_0^4 + \epsilon - \frac{2\delta}{3}\phi^n + \frac{1}{2}(\phi^n)^2\right)\phi^n \tag{3.16}$$

It is not difficult to see that equation 3.16 is the same as the internal iteration relation 3.9 save the positive definite operator of norm larger than unity (E) acting upon the time difference $\dfrac{\phi^{n,k+1}-\phi^{n,k}}{\tau}$

$$B \equiv E + \tau^2 L_{11}^{n,k} L_{22}^{n,k} \equiv E + O(\tau^2) \tag{3.17}$$

By considering the definition of the operators L_{ij} clearly operator B has no effect on the steady state result of the system. Furthermore the fact that $\|B\| > 1$ shows that the splitting scheme is more stable than the original implicit scheme with the same order of accuracy ($O(\tau^2)$).

3.2.4 Spatial discretization

For the discretization, a simple uniform mesh in both directions is used in a rectangular box defined as ($Rect := \{x \in [0, L_x], y \in [0, L_y]\}$), therfore

$$x_i = ih_x, \quad h_x = \frac{L_x}{N_x} \quad i = 0, \ldots, N_x \qquad y_j = jh_y, \quad h_y = \frac{L_y}{N_y} \quad j = 0, \ldots, N_y \tag{3.18}$$

where N_x and N_y are the number of points in x axis and y axis respectively. Consider $\phi_{i,j}$ the value of the function at the point (i, j). The simplest symmetric approximations for the fourth order derivatives existing in the model will be

$$\begin{aligned}
\Lambda_{11}\phi_{i,j} &= -\frac{\phi_{i-2,j} - 4\phi_{i-1,j} + 6\phi_{i,j} - 4\phi_{i+1,j} + \phi_{i+2,j}}{h_x^2} \approx -\frac{\partial^4}{\partial x^4} \stackrel{\text{def}}{=} L_{11}\phi \\
\Lambda_{22}\phi_{i,j} &= -\frac{\phi_{i,j-2} - 4\phi_{i,j-1} + 6\phi_{i,j} - 4\phi_{i,j+1} + \phi_{i,j+2}}{h_y^2} \approx -\frac{\partial^4}{\partial y^4} \stackrel{\text{def}}{=} L_{22}\phi \\
\Lambda_{12}\phi_{i,j} &= -\frac{1}{h_x^2 h_y^2}[\phi_{i-1,j-1} - 2\phi_{i-1,j} + \phi_{i-1,j+1} - 2(\phi_{i,j-1} - 2\phi_{i,j} + \phi_{i,j+1}) \\
&\quad + \phi_{i+1,j-1} - 2\phi_{i+1,j} + \phi_{i+1,j+1}] \approx -\frac{\partial^4}{\partial x^2 \partial y^2} \stackrel{\text{def}}{=} L_{12}\phi \\
\Lambda_1\phi_{i,j} &= -\frac{\phi_{i-1,j} - 2\phi_{i,j} + \phi_{i+1,j}}{h_x^2} \approx -\frac{\partial^2}{\partial x^2} \stackrel{\text{def}}{=} L_1\phi \\
\Lambda_2\phi_{i,j} &= -\frac{\phi_{i,j-1} - 2\phi_{i,j} + \phi_{i,j+1}}{h_y^2} \approx -\frac{\partial^2}{\partial y^2} \stackrel{\text{def}}{=} L_2\phi
\end{aligned} \tag{3.19}$$

Where Λ denotes the discrete approximation of each derivative operator. In this simulation, our domain is an incircle of a square box to have a better agreement with the experimental observations realized in TIPs[2] [31, 32]. As a consequence at each iteration we imposed the boundary condition by rendering $\phi_{i,j}$ at the gridpoints out of the circle equal to zero i.e. (I is the index set of the mesh)

$$\phi_{i,j} = 0 \quad \forall i, j \in I \quad \text{where} \quad \mathrm{x_i^2 + y_j^2} \geqslant \frac{\mathrm{a}^2}{2} \tag{3.20}$$

[2]Transfers, Interfaces and Processes laboratory of Université Libre du Bruxelles

in which a is the side length of the square. In §5.1 determinant role of boundary enclosing the systems in the formation of the patterns in the fluid layers will be discussed by using this circular boundary.

4 Knobloch Equation

4.1 Long-wave instability modes

Another class of models applying to different types of instabilities are those which describe cases where the primary instability of the system has a relatively large spatial scale in comparison with the other characteristic dimension of the problem. For instance in Bénard instability phenomena when both boundary of the system are heat-insulating as it was presented in §2.2 it is possible to have a uniform temperature increase throughout the system and there exist no force to restore the initial temperature of the system. It implies that system is neutrally stable for such homogeneous perturbations and therefore the dispersion relation of the system (obtained by linear stability analysis explained in §3.1) will possibly possess a zero root at $k_c = 0$.

By slowly tempering the system along its horizontal coordinate, system will be displaced from its neutral equilibrium and some dynamics is expected. It may imply a convection flow which possibly leads to instability of the horizontally stable state. Now considering a control parameter μ of such instability, the dispersion relation should adopt the form (coefficient of k^4 set to unity by suitable scaling of μ)

$$\sigma_{gr}(k,\mu) = k^2\mu - k^4 + O(k^6) \tag{4.1}$$

since the model equation should satisfy some symmetry and according to the assumption explained above

$$\forall\mu \quad \exists\sigma_{gr}(k,\mu) \quad \text{such that} \quad \sigma_{gr}(0,\mu) = 0$$

In order to extend the model to cases where the boundaries have a very small thermal conductivity such that homogeneous mode of equation equation (4.1) k itself has a slow evolution (assumed to be slow exponential damping here) it is possible to take into account a small term $-\alpha$ where $0 < \alpha \ll 1$.

Now the **linear part** of the model for conserved or quasi conserved scalar quantity ϕ consistent with (4.1) and complemented with the term α will read

$$\partial_t\phi = -\alpha\phi - \mu\Delta\phi - \Delta^2\phi \tag{4.2}$$

Above the instability threshold the nonlinear behaviour of the system requires accounting for nonlinearity. The form of nonlinearity is restricted by the symmetry considerations such as rotations ($\mathbf{r} \to R_\theta\mathbf{r}$), reflections ($\mathbf{r} \to M_\theta\mathbf{r}$) and translation in time ($\tau \to t+\Delta t$) and space ($\mathbf{r} \to \mathbf{r}-\mathbf{r}_0$). Moreover nonlinear terms are also subject to scaling considerations. For example, in the case of the system satisfying a strict invariance with respect to $\phi \to \phi + \tilde{\phi}$ ($\tilde{\phi}$ is small homogeneous perturbation, i.e. a uniform temperature

or depth variation as described above) all terms should be invariant to this transformation. As a consequence nonlinear terms such as ϕ^2 and ϕ^3 seen in SH model (3.1) cannot appear and $\alpha = 0$. On the other hand $(\nabla\phi)^2$ respects all the symmetries for small ϕ and no other nonlinear term can be found at this order thus yields the Kuramoto-Sivashinsky (KS) equation [2]

$$\partial_t\phi = -\mu\Delta\phi - \Delta^2\phi + (\nabla\phi)^2 \tag{4.3}$$

In order to allow weak dissipiation in the system hence breaking the strict invariance $\phi \to \phi + \tilde{\phi}$ ($\tilde{\phi}$, α will be inserted in the equation (4.3) and we will get the damped KS equation

$$\partial_t\phi = -\alpha\phi - \mu\Delta\phi - \Delta^2\phi + (\nabla\phi)^2 \tag{4.4}$$

Normand et al, Chapman and Proctor, Garcia-Ybarra, Castillo and Velarde also consider models to describe such nonlinear evolutions [2, 29] for different cases. Knobloch also proposed a general model [6] in 1990 for Bénard convection between undeformabl poorly heat-insulating boundaries in the limit of large Prandtl number which show very nice agreement with experiments [2]

$$\begin{aligned}\partial_t\phi = &- \alpha\phi - \mu\Delta\phi - \Delta^2\phi + \kappa\nabla.\left[(\nabla\phi)^2\nabla\phi\right] + \beta\nabla.\left[\Delta\phi\nabla\phi\right] + \\ &\delta\Delta\left[(\nabla\phi)^2\right] - \gamma\nabla.\left[\phi\nabla\phi\right]\end{aligned} \tag{4.5}$$

where γ quantifies non-Boussinesq effects and other parameters can be obtained for different particular problems(one-layer or two-layer system, buoyancy-driven or surface-tension-driven...).

In the present work we will consider a rescaled variant of this equation, taking into account the KS nonlinear term $(\nabla\phi)^2$, for the simulation of Marangoni-Bénard convection. Therefore the model is

$$\begin{aligned}\partial_t\phi = &\left[\tilde{\epsilon} - (1+\Delta)^2\right]\phi + \eta(\nabla\phi)^2 + \delta\Delta(\nabla\phi)^2 + \kappa\nabla.\left[(\nabla\phi)^2\nabla\phi\right] \\ &+ \beta\nabla.\left[\Delta\phi\nabla\phi\right] - \gamma\nabla.\left[\phi\nabla\phi\right]\end{aligned} \tag{4.6}$$

in which we rescale the Laplacian operator found in the SH model by $\Delta \to \dfrac{\Delta}{k_0^2}$ to be able to define a way to control the the typical wavenumber of the model and to have a ground for comparison between the modified Knobloch model and the model introduced in the SH model. Therefore by writing the dispersion relation by considering the linear part of the equation (4.6)

$$\sigma_{gr} = \tilde{\epsilon} - (1 - \frac{k^2}{k_0^2})^2 = (\tilde{\epsilon} - 1) + 2\frac{k^2}{k_0^2} - \frac{k^4}{k_0^4} = k_0^{-4}\left(k_0^4\left(\tilde{\epsilon} - 1\right) + 2k^2k_0^2 - k^4\right)$$

Then by equalising with growth relation for the SH model (3.4) and rescaling time (to cast aside the factor k_0^4)

$$k_0^4(\tilde{\epsilon}-1) = \epsilon - k_0^4$$
$$\Longrightarrow \quad \tilde{\epsilon} = \frac{\epsilon}{k_0^4} \tag{4.7}$$

Therefore by obtaining the relation between the supercriticality parameter in this model and its SH counterpart we will have a ground for the comparison. And as the previous case by considering k_0 and ϵ as linear functions in time, we would attempt to investigate the ramping of the system in time in our simulation.

For this reason a home made software developed by P. Colinet using C language based on **Fast Fourier Transform(FFT)** will be employed for the simulations. In what follows we will have a brief overview of this method.

4.2 Fast Fourier Transform method

Sometimes Fourier transform of an equation will bring notable simplicity to the structure of it and as a consequence the way to solve the equation. Numerical solution is not an exempt to this fact. Indeed for many models involving high order derivatives moving from the real space to Fourier space is highly recommended [30].

One can define the discrete Fourier transform and its inverse as follow (for a given function f, f_k is its value in the point k where $0 \leqslant k \leqslant N$ and $\tilde{f_n}$ is its corresponding Fourier transform)

$$\tilde{f_n} = \sum_{k=0}^{N-1} f_k exp(\frac{2\pi ikn}{N}) \tag{4.8}$$

$$f_k = \frac{1}{N}\sum_{k=0}^{N-1} \tilde{f_n} exp(\frac{2\pi ikn}{N}) \tag{4.9}$$

But how much computation is involved in the process of transform is the essential question which leads to the Fast Fourier Transform. Let's define $W^{n,k}$ as $W = exp(\frac{2\pi ikn}{N}$ hence $\tilde{f_n} = \sum_{k=0}^{N-1} W^{n,k} f_k$. Common sense suggests that ,considering the matrix $W \in M_{n*k}$ with $W^{n,k}$ as its component, the computation cost of the transform is of order $O(N^2)$. Though it is possible to prove that by rewriting the Fourier transform of the length N as the sum of two discrete Fourier transform of length $\frac{N}{2}$ one from the even number of points of N and the other one from the odd number of points like

$$\tilde{f} = \tilde{f_k^e} + W^{1,k}\tilde{f_k^o} \tag{4.10}$$

it is possible to calculate the transform in $O(Nlog_2\ N)$ operations which cause a remarkable optimization in the time of calculation for large database. There can be many modification to have more efficient method for decomposition of the Fourier transform (see [30]).

The idea behind the method used for solving the model (4.6) in our simulation is therefore solving linear part of the equation in Fourier space and frequency domain by employing fast Fourier transform and the nonlinear part in real space separately to avoid more complicated calculations related to their Fourier transform (e.g. convolution). After approximating of nonlinear part the result will be transformed to the Fourier space to be merged with the linear part and finally by an inverse transform to the time domain again the real solution will be achieved. This method has been used for many different models and it is one of the fastest model which sustains relatively high accuracy.

5 Results

5.1 Numerical results of Swif-Hohenberg equation

For the simulation of this model using the finite difference method explained in chapter §3 a C++ program has been developed using Eigen [33] library as the numerical solver. The Cholesky decomposition employed to deal with the system of equations arising from the implicit method in iteration. The typical result of the simulation for a circular domain inside a big square with the size of $a = 50$ therefore with the radius of 25 and using a mesh with 150×150 points from random initial condition produced by the random number generator introduced in [30] can be seen in Fig. 5.1.

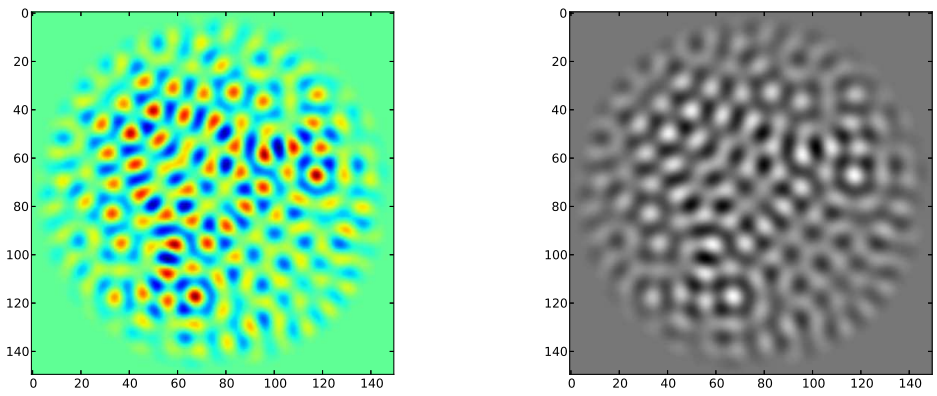

Figure 5.1: The snapshot of the system at unit time $t = 0.765$ with the typical wavenumber $k_0 = 1.1711$ for the model with the parameters $\epsilon = 0.1$ and $\delta = 1.3$ and $\tau = 10^{-3}$. The left image is a heat map of the solution where the redish regions denote the higher temperature. The right one represents the grayscale image of the same sample where the brighter regions have higher temperature

To illustrate Marangoni convective cells more clearly we will apply a **Voronoi diagram** to the image by which it will be simpler to recognise the effect of the boundaries and also the presence of different polygons in the result. Voronoi diagram or Voronoi decomposition is the technique that enables the division of space into subspaces. It involves P as a set of n distinct points (sites) in the plane and subdivide the plane into n cells one for each site by halving the hypothetical lines which connects each two neighbour points of P. The cells are the result of the intersection of these lines. We assume P is the set of local maxima of ϕ at the given time space. therefore the resulting cells of

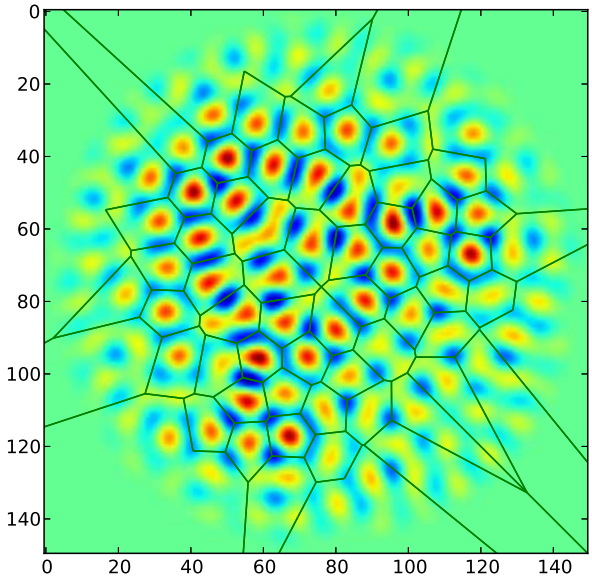

Figure 5.2: The polygonal convection cells captured by a Voronoi diagram

Voronoi diagram containing these points demonstrate the polygonal patterns expected as it is illustrated in Fig. 5.1. The effect of the boundary on the formation of patterns can be clearly recognised in this figure where the spatial structure of layer is strongly determined by the boundaries enclosing the system. Distorted hexagons are the dominant patterns in the system although few pentagons can be seen near the boundary.

Now in order to simulate the time-dependent patterns seen while the liquid thickness continuously decreases we will use the fact that supercriticality also decreases in time (given its definition based on Marangoni number (2.9) whereas the natural wavenumber should increase to account for the splitting of the convective cells. The variations of typical wavenumber and supercriticality is assumed to be linear and the system should be at its equilibrium state at the initial time i.e. considering the dispersion relation (3.4) $\epsilon - k_0^4 < 0$. We will increase k_0 from 1 to 5 and decrease ϵ from 0.9 to 0.1 throughout the simulation. Therefore

$$k_0 = 1 + \frac{4t}{T_{max}} \tag{5.1}$$

$$\epsilon = 0.9 - \frac{0.8t}{T_{max}} \tag{5.2}$$

where T_{max} is the endpoint of the time interval in which simulation will run hence slower change happens for larger T_{max}. The result for the case that $T_{max} = 500$ and for the circular boundary of the radius 15 with the resolution 150×150 can be seen in Fig.5.1

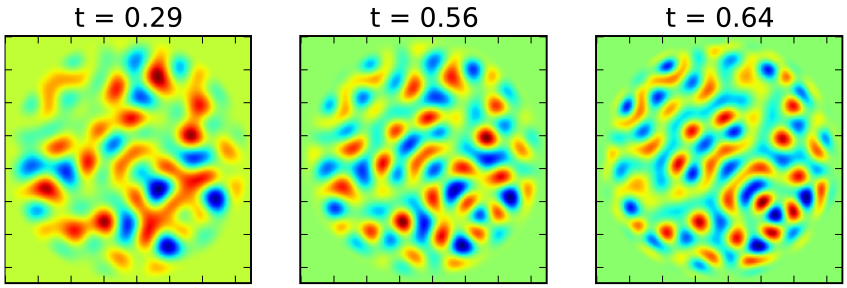

Figure 5.3: The snapshots of the system at three different time steps relatively close to each other with respect to T_{max} for the slowest change in k_0

We also run the simulation for the similar set-up with $T_{max} = 50$ and $T_{max} = 5$ to have faster evolution though even for the slowest case seen in Fig.5.1 the patterns evolve in time very fast and they strongly tend to damp which implies the need to validate the current implementation. Although qualitatively the splitting of the convective cells which was expected from theory and experiments can be recognized in this figure.

Despite the fair agreement of the results of the simulation with the experiments the program needs more validation for modelling more complex cases since by the current implementation it evolves very fast in time which is not very physical. Moreover it has the room for optimization to be more efficient (possibly by using faster numerical solvers and parallel computing methods) which will be considered for further improvement of implementation of the method for faster computations in near future. Nevertheless we were able to qualitatively observe the role of boundaries using these simulations and also the splitting of the convective cells in the thin liquid film which can be used in future studies of Bénard-Marangoni effect using Swift-Hohenberg model. This simulation has been in overall slower than the simulation of the modified Knobloch equation however the possibility of using circular boundary condition for the system is an advantage of the method used for numerical approximation of SH model.

5.2 Simulation results of Knobloch equation

For the simulation samples we consider Boussinesq situations with undeformable interfaces. Therefore in all the instances of the model simulation the parameter $\gamma = 0$ in the equation (4.6). Other coefficients of the nonlinear part of the system are considered to be constant and fixed as follows

$$\delta = -1.984 \qquad \kappa = 0 \qquad \beta = -0.331 \qquad \eta = 0$$

Therefore the nonlinear forces over the threshold act similarly for different cases giving the room for studying the effect of initial wavenumber and supercriticality on pattern

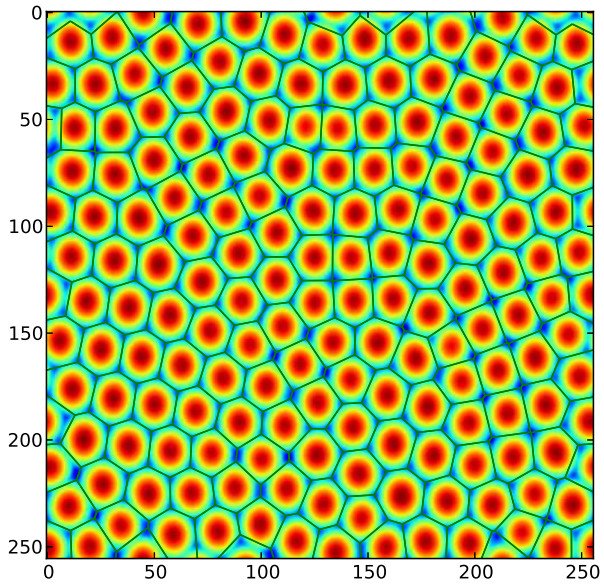

Figure 5.4: Marangoni convection cells in the simulation for $k_0 = 20$. Hexagons can be observed along with transition to squares and some heptagonal and pentagonal defects

formation in the domain. A typical result can be seen in Fig. 5.4 for $k_0 = 20$ and $Ma = 0.8$ and the resolution of 128×128 for a rectangular domain of $2\pi \times \frac{4\sqrt{3}\pi}{3}$ and with the random initial conditions generated by the built-in random generator of C.(Note that in this figure the y axis is scaled by the coefficient $\sqrt{3}/2$ for the sake of simplicity) In this figure polygonal patterns are captured by Voronoi diagram. Most of the patterns seen in this figure are relatively regular hexagons together with some defects in the form of pentagons and heptagons (and also typical features of the transition to square patterns which has a good qualitative agreement with the experiments).

We repeated the similar simulation with $k_0 = 8$ for different time increments till as large as $\Delta t = 0.5$ for the same resolution to test the convergence of the scheme. In order to analyse the data we use a statistical function called **power spectral density (PSD)** function which is widely used in statistical signal processing and physics. For this reason first the discrete Fourier transform $\tilde{\phi}_n(\mathbf{k})$ of ϕ_n (where n denotes the time step and $\mathbf{k} = (k_x, k_y)$) obtained from the simulation at the time step will be evaluated(see Fig. 5.5 demonstrate a state of the system in Fourier space)

Then PSD $Psd(k)$ can be defined as follows ($k_x = kcos\phi$ and $k_y = ksin\phi$)

$$Psd(\mathbf{k}) = \int_0^{2\pi} \tilde{\phi}(kcos\phi, ksin\phi)d\phi \tag{5.3}$$

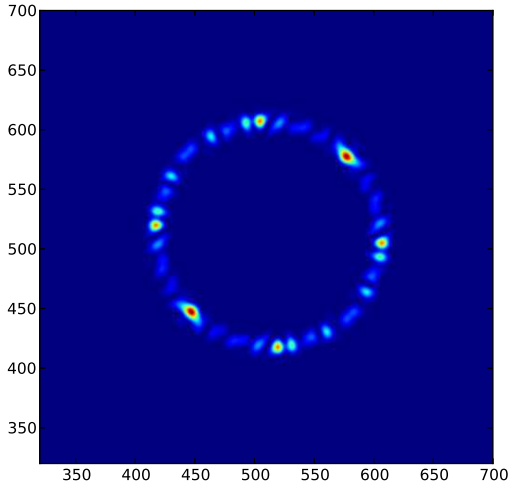

Figure 5.5: An example of the Fourier transform of the last state of the system in the simulation with $k_0 = 20$

which is indeed the distribution function of waves with different lengths(hence wavenumber) throughout the system. Fig... shows a sample plot of this function with respect to wavenumber. By considering this function it is possible to find the average value of the k_{max} at each time step which is in fact an approximation of k_0 in the relation(4.7) and can be used as a tool to analyse the simulation results. This average value can be obtained from the following equation

$$\overline{k}_{max} = \frac{\int_0^{k_{max}} \mathbf{k} Psd(\mathbf{k}) d\mathbf{k}}{\int_0^{k_{max}} Psd(\mathbf{k}) d\mathbf{k}} \tag{5.4}$$

There is another way to evaluate this average value by undertaking the Fourier transform of the solution at each time step to evaluate the local maxima of spectral density function and find the average value at each step with dividing the summation of them by the number of these local maxima. Therefore now by using this method the stability of the scheme can be realized By plotting ($\overline{k}_{max}$) with respect to time in Fig. 5.6 for different time increments. As the figure shows $\overline{k}_{max}$ after a finite time tends to a constant value

Interestingly this shows that the system does not only reach a steady state but also that the average of local maximum power densities and as a consequence the simulation results for $\Delta t = 0.1$ and $\Delta t = 0.5$ is quite similar after $t = 400$. Hence the simulation with relatively large strides (magnitude of time steps) can provide some qualitative information about the patterns. Another case considered is varying the natural wavenumber in the same resolution to have an intuition of possibility of varying the wavenumber by a function of time ($k_0(t)$) to be able to simulate the time-dependence nature of Marangoni

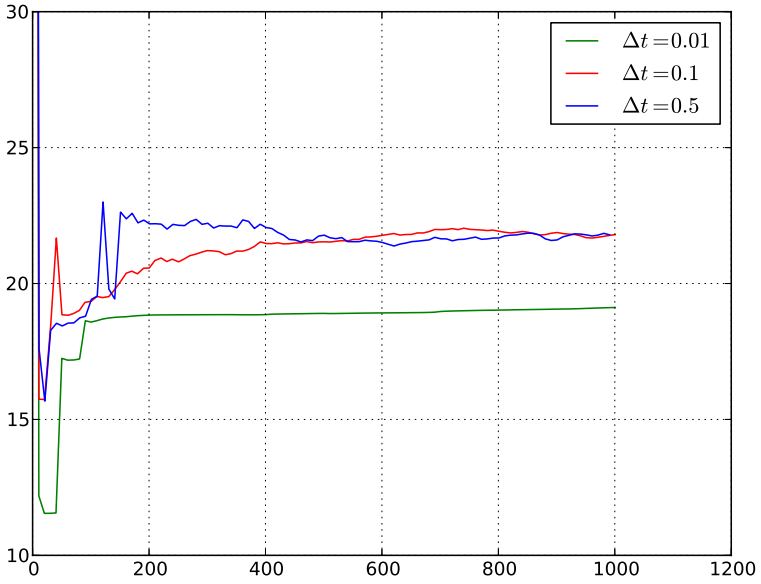

Figure 5.6: The comparison of the result for the simulation with the same parameter for different magnitude of time increment using PSD functions

cells in very thin liquid films. We will conduct the same power spectrum density analysis this time for different k_0

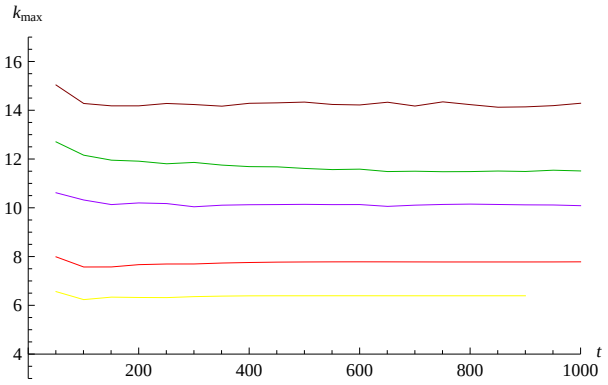

Figure 5.7: The comparison of the result for the simulation with different k_0 using local maximum of PSD at each time step for $\Delta t = 10^{-3}$. Brown line corresponds to results for $k_0 = 20$, green line denotes $k_0 = 16$, purple, red and yellow lines representing the results for $k_0 = 12$, $k_0 = 10$, $k_0 = 8$ respectively

The convergence to a steady state can be recognized in the Fig. 5.7. Note that at

larger value of $k_0 > 20$ stripes are dominant in visualization of the results.

Now we are equipped to deal with the time-dependent evolution of patterns in thin liquid films. We will increase k_0 from 2 to 12 linearly by time while linearly decreasing the supercriticality from 0.8 to 0.3. Providing the fact that the system at initial time is in equilibrium state which means $\tilde{\epsilon} - k_0^4 < 0$ we will introduce the functions for ramping the system. (T_{max} is representing the endpoint of time interval in which the simulation will run)

$$k_0 = 2 + \frac{10}{T_{max}} t \tag{5.5}$$

$$\tilde{\epsilon} = 0.8 - \frac{1}{2T_{max}} t \tag{5.6}$$

The speed of evolution of the patterns hence will be determined by changing T_{max}. Therefore we run simulation for three different speed of ramping namely fast ($T_{max} = 100$) Fig.5.8, moderate speed ($T_{max} = 200$) Fig.5.9 and finally pattern evolution with slow pace($T_{max} = 500$) Fig.5.10. As it can be seen in these images, The model successfully captures the time evolving nature of convection cells in time. At the start of the simulation from the random initial condition, the formation of cells can be seen and in all three cases over the time interval the splitting of the cells complying with the experimental observations.

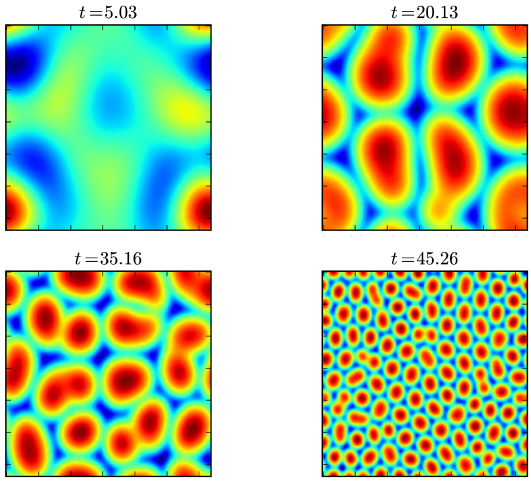

Figure 5.8: Snapshot of the systerm at different time units $t \in [0, 100]$ to show the fast evolution of Marangoni convection cells in the 100 unit of time

Now we will employ PSD analysis once again to check if the $\overline{k}_{max}$ obtained from the equation (5.4) will be close to the linear evolution of k_0 in the model equation. Fig 5.11

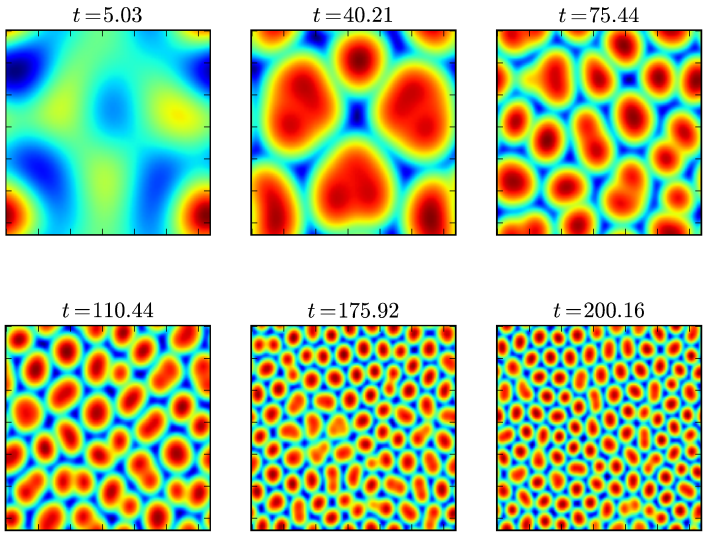

Figure 5.9: Snapshot of the Marangoni convection cells developing and evolving in time interval $t \in [0, 200]$ with moderate speed

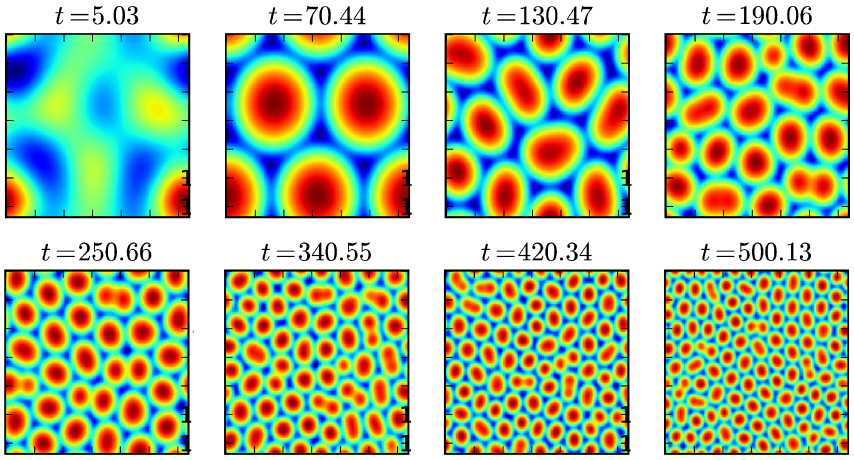

Figure 5.10: Snapshot of the systerm at different time units ($t \in [0, 500]$) to show the slow evolution of Marangoni convection cells in the 500 units of time

demonstrate that $\overline{k}_{max}$ in all the instance simulations increase in time quite close to the line which shows the linear evolution of k_0 in the model implying a relatively accurate

numerical solutions using the FFT method. Hence the distribution of solutions yields a power spectrum that coincides within the accuracy of our calculations possibly related to the rotation of the patterns in the domain, with that given by direct variation of the typical wavenumber.

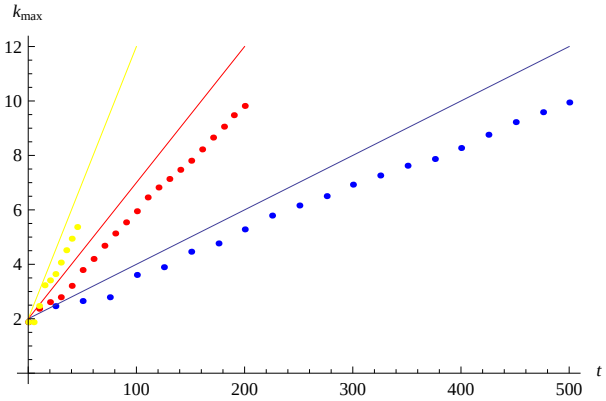

Figure 5.11: Comparison between evolution of $\overline{k}_{max}$ obtained from the simulation datas in time which are denoted by color circle and its corresponding linear increasing line of k_0 in time. Yellow, red circles and blue are respectively showing fast, moderate and slow pattern evolution and their line counterparts are representing the k_0 equation with the same order

Although we could not treat the model in circular domain with FFT method, in this latter case the results are very promising and it is credible enough to be used for the comparison with the real time experiments and investigating of the pentagon-heptagon defects for the nucleation of the new convection cells. It is also conceivable as mentioned before by some assumption to use this model for simulating the solutal Bénard-Marangoni convection which have wide range of applications in nano particle depositions and polymer coating and....

Conclusion and possible future perspectives

In this thesis after a general introduction to Bénard-type patterns and notion of instabilities and the applications of such a study in connection with a wide range of disciplines in science and technology, two very popular simplified models for non-equilibrium patterns have been studied in order to understand mostly fundamental aspects of wave and pattern formation in such systems. These models can be derived from the governing equations of fluid dynamics using some asymptotic analysis technique (small super-criticality ϵ, rescaling, long-wave expansions, ...).

The first model considered is a variation of celebrated Swift-Hohenberg equation introduced by P. C. Hohenberg and J. B. Swift in 1977, which is a nonlinear parabolic equation containing fourth-order space derivatives.This model describes Bénard-Marangoni convection at least qualitatively and it monotonically evolves in time to a steady state which minimizes some energy functional (Lyapunov functional). A semi-implicit finite-difference scheme has been developed for this model based on the operator-splitting method and using internal iteration to deal with nonlinearity considering a circular boundary in a square box (as used in the earlier experiments realized in TIPs [1]). This scheme was initially proposed by C. I. Christov and J. Pontes in 2001. In addition, the model has been modified to account for the decreasing depth characteristic of the evaporative layer during the evolution in time, by prescribing the time evolution of some parameters measuring the typical wavenumber and the supercriticality of the liquid layer.

The other model which has been discussed in this study is Knobloch generalization of the works of G. I. Sivashinsky and Garcia-Ybarra et al. Knobloch equation indeed describes the nonlinear evolution of fluctuations (temperature deviations from the conductive profile) of very small wavenumber compared to other characteristic dimensions of the problem. He proposed this equation for Bénard convection between poorly conducting undeformable boundaries, and in the limit of large Prandtl number (the ratio of momentum diffusivity and thermal diffusivity). For the numerical simulation of this equation the Fast Fourier Transform (FFT) method has been previously implemented by P. Colinet, and it is briefly explained and employed for the simulation of the pattern formation. Again, we have modified it for ramping the system in time, to take into account the change in the layer depth in the process of evaporation.

Finally a succinct qualitative comparison between the outcome of these simulation and the results of experimental observation found in the literature (or obtained at TIPs) has been made.

As a future perspective a comparison can be made between the results of these two simulations based on careful assumptions for more accurate investigation. Further stud-

[1] Transfers, Iterfaces and Processes department of Université Libre du Bruxelles

ies could be done for improvement in computational efficiency of the finite-difference scheme and also for more precise characterization of the function accounting for the change of parameters of the models in time, in order to illustrate a stronger resemblance with experiments particularly as far as the patterns induced by drying in liquid films are concerned.

Acknowledgement

The author would like to thank Prof. Pierre Colinet for his tremendous support and supervision during the course of preparation of this master thesis and for giving the opportunity to use the facilities of TIPs laboratory of ULB. Special thanks goes to Prof. Bruno Rubino and Prof. Jaroslaw Rybicki without whom last two years would not have been so rich both scientifically and culturally. At the end the author gratefully acknowledge the financial support of European Commission through the Erasmus Mundus master program in mathematical modelling in engineering: theory, numerics and applications (Mathmods).

Bibliography

[1] P. Colinet, J. C. Legros, M. G. Velarde, *Nonlinear Dynamics of Sureface-Tension-Driven Instabilities*, Wiley-VCH, 1st edition (2001)

[2] P. Colinet and A. Nepomnyashchy, *Pattern Formation at Interfaces*, Springer Vienna (2010)

[3] P. C. Hohenberg and J. B. Swift, *Hydrodynamic fluctuations at the convective instability*, Phys. Rev. A 15, 319 (1977).

[4] L. Gelens and E. Knobloch. Traveling waves and defects in the complex Swift-Hohenberg equation. Phys. Rev. E. 84 056-203 (2011)

[5] C. I. Christov and J. Pontes, *Numerical scheme for Swift-Hohenberg equation with strict implementation of lyapunov functional*, Mathematics and Computer Modeling 35 (2002) 0895-7177, 87–99.

[6] E. Knobloch, *Pattern selection in long-wavelength convection*, Physica D. 41, 450-479 (1990)

[7] I. Prigogine, *Introduction to thermodynamics of Irreversible processes*,Wiley ,1961

[8] L. Perko *Differential Equations and Dynamical Systems*, Springer, 3rd edition 2000

[9] R. Seydel,*From Equilibrium to Chaos: Practical Bifurcation and Stability Analysis*, Elsevier, 1988.

[10] , A. M. Turing, *The Chemical Basis of Morphogenesis*, Jstor, 1952

[11] G. Nicolis, *Introduction to Nonlinear Science*, Cambridge University Press, 1995

[12] M. C. Cross, P. C. Hohenberg, *Pattern formation outside of equilibrium*, Rev. Mod. Phys. 65, 8511112 (1993)

[13] E. Bodenschatz, W. Pesch, G. Ahlers, *Recent Developments In Rayleigh-Bnard Convection*, Annu. Rev. Fluid Mech. 32, 709778 (2000)

[14] W. Wang,Y. Cali, M. Wu, K. Wang, Z. Li, *Complex dynamics of a reactiondiffusion epidemic model* ,Journal of Nonlinear analysis 2009

[15] M. Cross, H. Greenside, *Pattern Formation and Dynamics in Nonequilibrium Systems*, Cambridge University Press, 2009

[16] M. Maillard, L. Motte, A. T. Ngo, and M. P. Pileni, *Rings and Hexagons Made of Nanocrystals: A Marangoni Effect*, J. Phys. Chem. B 2000, 104, 11871-11877

[17] W.A. Tokaruk, T.C.A. Molteno and S.W. Morris, *BénardMarangoni convection in two-layered liquids*, Phys. Rev. Lett. 84, 35903593 (2000)

[18] M. Dondlinger, J. Margerit and P.C. Dauby *Weakly nonlinear study of Marangoni instabilities in an evaporating liquid layer*, J. Colloid and interface science, 283 522532 (2005)

[19] S.J. VanHook, M.F. Schatz, J.B. Swift, W.D. McCormick and H.L. Swinney, *Long-wavelength surface-tension-driven Bénard convection: experiment and theory*, J. Fluid Mech. 345, 45 (1997).

[20] R. D. Deegan, O. Bakajin, T. F. Dupont, G. Huber, S. R. Nagel and T. A. Witten, *Capillary flow as the cause of ring stains from dried liquid drops*, Nature 389, 827829 (1997)

[21] H. Hu, R. Larson, *Marangoni Effect Reverses Coffee-Ring Depositions*, J. Physical chem. 110, 70907094 (2006)

[22] M.A. Mendes-Tatsis and E.S. Perez de Ortiz, *Spontaneous interfacial convection in liquid-liquid binary systems under microgravity*, Proc. R. Soc. London A 438, 389396 (1992).

[23] M.A. Mendes-Tatsis and E.S. Perez de Ortiz, *Marangoni instabilities in systems with an interfacial chemical reaction*, Chem. Eng. Sci. 51, 3755 (1996).

[24] O. Kabov, B. Scheid, I.V. Marchuk and J.C. Legros, *Free surface deformation by thermocapillary convection in a moving thin liquid layer locally heated*, J. of the Russian Academy of Sciences, Mechanics of Fluids and Gases (2001)

[25] M. Majumder, C. S. Rendall, J. A. Eukel, J. Y. L. Wang, N. Behabtu, C. L. Pint, T. Liu, A. W. Orbaek, F. Mirri, J. Nam, A. R. Barron, R. H. Hauge, H. K. Schmidt and M. Pasquali, *Overcoming the "Coffee-Stain" Effect by Compositional Marangoni-Flow-Assisted Drop-Drying*, J. Phys. Chem. B 116, 65366542 (2012)

[26] V. Petrov, M.F. Schatz, K.A. Muehlner, S.J. VanHook, W.D. McCormick, J.B. Swift and H.L. Swinney, *Nonlinear control of remote unstable states in a liquid bridge convection experiment*, Phys. Rev. Lett. 77, 37793782 (1996).

[27] C.I. Christov, J. Pontes, D. Walgraef and M.G. Velarde, *Implicit time splitting for fourth-order parabolic equations*, Comp. Meth. Appl. Mech. and Eng. 148, 209-224 (1997).

[28] J. Douglas and H.H. Rachford, *On the numerical solution of heat conduction problems in two and three space variables*, tins. Amer. Math. Sot. 82, 421-439 (1956).

[29] D. Zhengde, J. Murong, *Existence Time of Solution of the (1+2)D Knobloch Equation with Initial-Boundary Value Problem*, Acta Mathematica, 20B (4) 451-460 (2000)

[30] W. H. Press, S. A. Teukolsky, W. T. Vetterling and B. P. Flannery, *Numerical Recipes The Art of Scientific Computing*, Cambridge University Press 3rd Edition (2009)

[31] F. Chauvet, S. Dehaeck and P. Colinet, *Threshold of Bnard-Marangoni instability in drying liquid films*, Europhys. Lett. 99, 34001 (2012).

[32] P. Colinet, F. Chauvet and S. Dehaeck, *Genesis of Bnard-Marangoni patterns in thin liquid films drying into air*, to appear in *Without bounds: a scientific canvas of nonlinearity and complex dynamics*, Eds: R. G. Rubio, Yu. S. Ryazantsev, V. M. Starov, G. X. Huang, A. P. Chetverikov, P. Arena, A. A. Nepomnyashchy, A. Ferrús and E. G. Morozov, Springer-Verlag (2012).

[33] http://eigen.tuxfamily.org/

[34] http://hamshahrionline.ir/details/159347

[35] http://blogs.discovermagazine.com/80beats/2011/08/17/why-do-coffee-rings-form-because-the-grounds-are-round/